The Astrophysical Journal, 856:72 (12pp), 2018 March 20
https://doi.org/10.3847/1538-4357/aaa1f1

An Extreme Protocluster of Luminous Dusty Starbursts in the Early Universe

I. Oteo[1,2], R. J. Ivison[1,2], L. Dunne[1,3], A. Manilla-Robles[2,4], S. Maddox[1,3], A. J. R. Lewis[1], G. de Zotti[5], M. Bremer[6], D. L. Clements[7], A. Cooray[8], H. Dannerbauer[9,10], S. Eales[3], J. Greenslade[7], A. Omont[11,12], I. Perez–Fournón[8,9], D. Riechers[13], D. Scott[14], P. van der Werf[15], A. Weiss[16], and Z-Y. Zhang[1,2]

[1] Institute for Astronomy, University of Edinburgh, Royal Observatory, Blackford Hill, Edinburgh EH9 3HJ, UK; ivanoteogomez@gmail.com
[2] European Southern Observatory, Karl-Schwarzschild-Str. 2, D-85748 Garching, Germany
[3] School of Physics and Astronomy, Cardiff University, The Parade, Cardiff CF24 3AA, UK
[4] Department of Physics and Astronomy, University of Canterbury, Private Bag 4800, Christchurch, 8140, New Zealand
[5] INAF, Osservatorio Astronomico di Padova, Vicolo Osservatorio 5, I-35122 Padova, Italy
[6] H. H. Wills Physics Laboratory, University of Bristol, Tyndall Avenue, Bristol BS8 1TL, UK
[7] Physics Department, Blackett Lab, Imperial College, Prince Consort Road, London SW7 2AZ, UK
[8] Department of Physics and Astronomy, University of California, Irvine, CA 92697, USA
[9] Instituto de Astrofísica de Canarias (IAC), E-38205 La Laguna, Tenerife, Spain
[10] Universidad de La Laguna, Dpto. Astrofísica, E-38206 La Laguna, Tenerife, Spain
[11] CNRS, UMR 7095, Institut d'Astrophysique de Paris, F-75014, Paris, France
[12] UPMC Univ. Paris 06, UMR 7095, Institut d'Astrophysique de Paris, F-75014, Paris, France
[13] Cornell University, Space Sciences Building, Ithaca, NY 14853, USA
[14] Department of Physics and Astronomy, University of British Columbia, Vancouver, BC V6T 1Z1, Canada
[15] Leiden Observatory, Leiden University, P.O. Box 9513, NL-2300 RA Leiden, The Netherlands
[16] Max-Planck-Institut für Radioastronomie, Auf dem Hügel 69 D-53121 Bonn, Germany

Received 2017 September 7; revised 2017 October 31; accepted 2017 November 22; published 2018 March 26

Abstract

We report the identification of an extreme protocluster of galaxies in the early universe whose core (nicknamed Distant Red Core, DRC, because of its very red color in *Herschel* SPIRE bands) is formed by at least 10 dusty star-forming galaxies (DSFGs), spectroscopically confirmed to lie at $z_{\rm spec} = 4.002$ via detection of [C I](1–0), ^{12}CO(6–5), ^{12}CO(4–3), ^{12}CO(2–1), and $H_2O(2_{11}–2_{02})$ emission lines with ALMA and ATCA. These DSFGs are distributed over a 260 kpc × 310 kpc region and have a collective obscured star formation rate (SFR) of $\sim$6500 $M_\odot$ yr^{-1}, considerably higher than those seen before in any protocluster at $z \gtrsim 4$. Most of the star formation is taking place in luminous DSFGs since no Lyα emitters are detected in the protocluster core, apart from a Lyα blob located next to one of the DRC components, extending over 60 kpc. The total obscured SFR of the protocluster could rise to SFR $\sim$ 14,400 $M_\odot$ yr^{-1} if all the members of an overdensity of bright DSFGs discovered around DRC in a wide-field Large APEX BOlometer CAmera 870 μm image are part of the same structure. [C I](1–0) emission reveals that DRC has a total molecular gas mass of at least $M_{\rm H_2} \sim 6.6 \times 10^{11}\,M_\odot$, and its total halo mass could be as high as $\sim 4.4 \times 10^{13}\,M_\odot$, indicating that it is the likely progenitor of a cluster at least as massive as Coma at $z = 0$.

Key words: galaxies: clusters: general – galaxies: evolution – galaxies: high-redshift – radio lines: ISM – submillimeter: galaxies – submillimeter: ISM

1. Introduction

Protoclusters of galaxies are key to tracing the formation of the most massive dark-matter halos in the universe and represent excellent laboratories in which to confront cosmological simulations (Borgani & Kravtsov 2011) as well as tools to test and constrain cosmology (Allen et al. 2011; Harrison & Coles 2012). Furthermore, whereas the contribution of cluster of galaxies to the cosmic star formation rate (SFR) density (Madau & Dickinson 2014) in the local universe is very low, the contribution of protoclusters might represent up to $\sim$25% at $z \sim 4$ and $\sim$50% at $z \sim 10$. In parallel, the fractional cosmic volume occupied by protoclusters increases by three orders of magnitude from $z \sim 0$ to $z \sim 7$ (Chiang et al. 2017). All this highlights the importance of protoclusters in the early universe for our understanding of galaxy and structure formation and hierarchical growth (Overzier 2016).

A ubiquitous feature of galaxy clusters up to $z \sim 2$ is the presence of a strong red sequence produced by massive, passively evolving early-type galaxies, which dominate their cores (see, e.g., Bremer et al. 2006; Stanford et al. 2006; Hilton et al. 2009; Rosati et al. 2009). The bulk of their star formation occurred at $z > 2$, over relatively short periods, in a phase compatible with luminous dusty star-forming galaxies (DSFGs—e.g., Casey et al. 2014) at $z > 3$–4 (Collins et al. 2009; Thomas et al. 2010; Gobat et al. 2011; Zeimann et al. 2012). Consequently, the average total SFR in galaxies that go on to populate rich cluster cores might reach several $\times 1000\,M_\odot$ yr^{-1} (for a Salpeter stellar initial mass function, IMF, though see Romano et al. 2017) for the most massive examples during the early stages. This implies that developing protoclusters might be identifiable as sub-megaparsec regions with multiple submillimeter-bright DSFGs with total SFRs of thousands of $M_\odot$ yr^{-1}. Such structures have already been found up to $\sim$3 (e.g., Ivison et al. 2013; Dannerbauer et al. 2014; Umehata et al. 2014, 2015; Yuan et al. 2014; Casey et al. 2015; Flores-Cacho et al. 2016; Hung et al. 2016; Planck Collaboration et al. 2016; Wang et al. 2016) but those reported at $z \gtrsim 4$ are much less extreme and typically contain only one DSFG (Daddi et al. 2009; Capak et al. 2011; Walter et al. 2012).

As a result of our systematic search for ultrared DSFGs (sources whose SPIRE flux densities increase from 250 to 500 μm—Ivison et al. 2016) in the *H*-ATLAS survey

(Eales et al. 2010), we discovered one system with exactly those characteristics, which is therefore the ideal observational model of the early evolution of protoclusters. This source was nicknamed the Distant Red Core (DRC, R.A. = 00:42:23.8, decl. = −33:43:34.8), and it might represent the core of a larger protocluster of galaxies at $z_{\rm spec} = 4.002$. This nickname reflects the fact that this was the reddest source found in *H*-ATLAS with $S_{250} < S_{350} < S_{500} < S_{870}$. Consequently, it was initially thought to lie at very high redshift, $z \sim 5$–6, according to its photometric redshift (Ivison et al. 2016). For this reason, most of the initial follow-up was designed to detect CO lines at those redshifts.

In this paper, we report on the nature of this unique system, along with the observations that led to its discovery. The paper is organized as follows: Section 2 describes the observations used in this work. Section 3 reports the discovery of this unique system, and then in Section 4 we discuss its physical properties, including SFR, molecular gas mass, total mass (baryonic and dark matter), and gas-depletion time. Finally, Section 5 presents the main conclusions of the paper. The total IR luminosities ($L_{\rm IR}$) reported in this work refer to the integrated luminosities between rest-frame 8 and 1000 μm, and the SFRs are derived from $L_{\rm IR}$ by assuming a Salpeter IMF and the classical Kennicutt (1998) calibration. Throughout the paper, we assume a ΛCDM cosmology with $H_0 = 70$ km s^{-1} Mpc^{-1}, $\Omega_\Lambda = 0.7$, and $\Omega_{\rm M} = 0.3$.

2. Observations

2.1. APEX Observations

DRC was observed with The Atacama Pathfinder Experiment (APEX) telescope's Large APEX BOlometer CAmera (LABOCA—Kreysa et al. 2003; Siringo et al. 2009) at 870 μm as part of a program aimed at looking for overdensities of dusty starbursts around ultrared DSFGs (Lewis et al. 2017). The APEX observations for DRC were carried out during 2013 October under projects M-092.F-0015-2013 (P.I. A. Weiss) and 191A-0748 (P.I. R. J. Ivison). A compact-raster scanning mode was used, whereby the telescope scans in an Archimedean spiral for $t_{\rm int} = 35$ s at four equally spaced raster positions in a $27'' \times 27''$ grid. Each scan was approximately $t_{\rm int} \approx 7$ minutes long such that each raster position was visited three times leading to a fully sampled map over the full 11′-diameter field of view of LABOCA. During the observations, we recorded typical precipitable water vapor (PWV) values between 0.4 and 1.3 mm, corresponding to a zenith atmospheric opacity of $\tau = 0.2$–0.4. Finally, the flux density scale was determined to an rms accuracy of $\sigma_{\rm calib} \approx 7\%$ using observations of the primary calibrators, Uranus and Neptune, while pointing was checked every hour using nearby quasars and found to be stable to $\sigma_{\rm point} \approx 3''$ (rms). A total of 11.4 hr were spent integrating on our target, covering an area of 124 arcmin^2. The final map was then beam-smoothed, to a resolution of 27″. The average rms background noise is then ∼1.9 mJy beam^{-1}. The data were reduced using the Python-based BOlometer data Analysis Software package (BOA v4.1—Schuller 2012), following the prescription outlined in Siringo et al. (2009) and Schuller et al. (2009). More details about the observations, data reduction and source extraction can be found in Lewis et al. (2017).

2.2. ALMA Observations

The ALMA data presented in this paper come from four different projects: 2013.1.00449.S (P.I. A. Conley), 2013.A.00014.S—a Director's Discretionary Time (DDT) proposal (P.I. R. J. Ivison), 2013.1.00001.S (P.I. R. J. Ivison), and 2016.1.01287.S (P.I. I. Oteo).

In project 2013.1.00449.S, we carried out spectral scans in the 3 mm band on a sample of eight ultrared starbursts at $z_{\rm phot} \gtrsim 4$ selected from HerMES (Oliver et al. 2012) and *H*-ATLAS surveys with the aim of measuring their redshift via multiple CO line detections (Asboth et al. 2016; Oteo et al. 2016b; Fudamoto et al. 2017; Riechers et al. 2017). The observations were taken between 2014 July 03 and August 28, in a total of five scheduling blocks (SBs) corresponding to the five tunings needed to cover most of ALMA band 3, between 84 and 114.88 GHz. The data for each SB were reduced in CASA, following standard procedures. Imaging was carried out using natural weighting to improve sensitivity, resulting in an average rms sensitivity of ∼0.75 mJy beam^{-1} in channels binned to 100 km s^{-1}. The FWHM synthesized beam ranged between 0.″6 and 1.″2 due to the different array configurations used in the different tunings.

In project 2013.A.00014.S, we observed DRC for about one hour, aiming to confirm what were thought to be two faint emission lines, ^{12}CO(7–6) and [C I] (2–1), detected in DRC at around 98.4 GHz in data from the earlier project, 2013.1.00449.S.[17] The observations were carried out on 2015 January 14, when the array was in a compact configuration. The data were reduced using the ALMA pipeline and imaged using natural weighting to improve sensitivity. The resulting beam size was ∼2.″0 FWHM and the rms sensitivity was ∼0.13 mJy beam^{-1} in 100 km s^{-1} channels.

Project 2013.1.00001.S consisted of high-spatial-resolution (0.″12) continuum observations of the brightest DRC component, what we will call DRC-1, at 870 μm. The aim of the observations was to study the morphology and extent of the dust emission in a subsample of the ultrared DSFGs presented in Ivison et al. (2016). Details on the observations, data calibration, and imaging can be found in Oteo et al. (2016b, 2017b). Briefly, the data were calibrated using the ALMA pipeline and imaging was done using Briggs weighting, which represents a good compromise between depth and spatial resolution. The resulting rms sensitivity is ∼0.1 mJy beam^{-1} with an FWHM synthesized beam of ∼0.″12 or ∼830 pc at $z = 4.002$.

In project 2016.1.01287.S, we observed DRC at 2 mm in 14 SBs, each about 70 minutes long, with the aim of detecting one or more additional emission lines to determine the redshift of DRC unambiguously. Due to the smaller primary beam in band 4, a two-pointing mosaic was used, such that roughly the same area was covered as for the earlier 3 mm observations, without significant primary beam attenuation. The data were calibrated using the ALMA pipeline and imaging was done using natural weighting in the concatenated visibilities corresponding to the two pointings. The resulting rms sensitivity is ∼50 μJy beam^{-1} in 100 km s^{-1} channels and ∼6 μJy beam^{-1} in the continuum map, with a synthesized beam size (FWHM) of 1.″68 × 1.″54 in both pointings.

---

[17] As we see later, these two putative lines were revealed to be one extremely broad line, namely [C I] (1–0).

2.3. Jansky VLA Observations

We used the Karl G. Jansky Very Large Array (VLA) to observe DRC, covering 27.68–28.58 GHz and 32.01–32.90 GHz using the 8-bit samples, in the CnB configuration, during 2015 January 24–25 (project VLA/14B-497; P.I. R. J. Ivison). The data were calibrated using the VLA pipeline, and the calibrated visibilities were imaged using natural weighting to improve the sensitivity. These observations were aimed at detecting low-*J* CO lines from DRC, but after the redshift was confirmed with the ALMA and ATCA observations, we knew that no CO lines were covered by the VLA spectral setup. Therefore, we utilize only the continuum map in this paper, which has an rms sensitivity of ∼6.3 μJy beam^{-1} and a synthesized beam (FWHM) of 1$''$07 × 0$''$66.

2.4. VLT Observations

DRC was observed on the nights of 2015 August 13, and September 5 and 7 with the Multi Unit Spectroscopic Explorer (MUSE) integral field spectrograph mounted on the European Southern Observatory's Very Large Telescope UT4 (Bacon et al. 2010; DDT program 295.A-5029, P.I. I. Oteo), with a seeing varying between 0$''$9 and 1$''$1. The 1$'$ × 1$'$ MUSE field of view was centered on the protocluster core, covering the 11 components detected in our ALMA Cycle 4 observations. With the nominal wavelength range (475–930 nm), we performed a series of exposures, each 15 minutes, for a total on-source time of 3 hr. Between individual exposures, the spectrograph was rotated by 90° and a random dithering pattern was added. The data were reduced using the MUSE pipeline, which performed all the basic reduction steps (Bacon et al. 2015). The subtraction of the sky emission was improved in the reduced cubes using a set of custom scripts.

FORS2 broadband imaging in the *I* filter were carried out during 4 h on the night of 2014 December 17 (project 093.A-0705, P.I: R. J. Ivison) under good weather conditions with seeing ∼1$''$. The data were reduced with the ESOREX pipeline following the standard procedures and the final images were astrometrically calibrated using the available VIKING *z*-band imaging in the field. The observations reached a 5σ limiting magnitude of 25.3 mag.

2.5. Gemini Observations

Broadband near-IR observations in the K_s filter were carried out between 2014 July 18 and November 04 with FLAMINGOS-2 mounted in the Gemini-South telescope (project GS-2014A-Q-58, P.I. L. Dunne). DRC was observed for a total of 4.1 h with an average seeing of 0$''$72. A classical dither pattern was used to remove the sky emission during the data reduction, performed with THELI (Schirmer 2013). First, the flat-field and dark correction was applied to each science frame, then the sky emission in each science frame was subtracted using a dynamical model of four images taken immediately before and after each frame. The flat-field correction was applied, cosmic rays were removed and the vignetted region of the image was masked. Finally, the images were combined using SWarp (Bertin 2010) and astrometrically corrected and flux calibrated using 2MASS (Skrutskie et al. 2006). The final image has a 3σ limiting magnitude of 25.03 mag in a 2$''$ aperture.

2.6. Spitzer/IRAC

DRC was observed with *Spitzer*/IRAC at 3.6 and 4.5 μm on 2015 September 14 (program ID: 11107; PI: Pérez-Fournon). A 36-position dither pattern with 30 s exposures per frame was used, totaling 1080 s integrations in each band. Data reduction was performed with the *MOPEX* package using standard procedures. Absolute astrometry was obtained relative to *Gaia* DR1, yielding rms accuracies of 0$''$04 and 0$''$06 in the 3.6 and 4.5 μm bands, respectively.

2.7. ATCA Observations

The ^{12}CO(2–1) emission from DRC was observed with the Australia Telescope Compact Array (project C3185, P.I. I. Oteo) during 2017 July 18–19 in its most compact configuration, with the 64 MHz spectral mode. The setup of the observations was carried out using the calibrator 1921−293, which was also used for bandpass calibration. The absolute flux scale (which we estimate to have an uncertainty of ∼15%) was determined by observing 1934−638, while 0104−408 was used as the phase calibrator. The observations were carried out in good weather conditions and covered almost full tracks, for a total on-source time of ∼14 hr. The data were calibrated by using the standard techniques in MIRIAD, including manual flagging of bad data (note that antenna CA06 was used in the observations but these data were flagged after the calibration was complete due to the poor data quality with respect to the other antennas). The calibrated visibilities were then transformed into CASA format, where the cubes and continuum maps were created by using natural weighting to improve sensitivity. The resulting synthesized beam FWHM is 14$''$2 × 10$''$6 and the rms sensitivity is ∼0.13 mJy beam^{-1} in ∼800 km s^{-1} wide channels.

Continuum observations with ATCA at 32.5, 9.0, and 5.5 GHz were carried out between 2013 October and 2015 July (project C2905, P.I. L. Dunne). The 7 mm observations were initially aimed at confirming the redshift of DRC via detection of ^{12}CO, but no lines were detected and thus we only use the continuum maps here. The data were reduced in MIRIAD following standard procedures, then the continuum maps were created from the calibrated visibilities in CASA. At 32.5 GHz the continuum map reached an rms sensitivity of ∼7.6 μJy beam^{-1} with a synthesized beam (FWHM) of 1$''$3 × 0$''$7. The observations at 9.0 and 5.5 GHz reached rms sensitivities of ∼6.6 μJy beam^{-1}.

3. An Extreme Overdensity of DSFGs

The wide-field LABOCA map at 870 μm (see left panel of Figure 1) revealed a $2.15^{+0.8}_{-0.5}\sigma$ overdensity (see Lewis et al. 2017 for details) of DSFGs with respect to the most recent single-dish number counts at 870 μm (Geach et al. 2017). The brightest DSFG of this overdensity (components A and B in the left panel of Figure 1, which form an extended 870 μm source) was followed up with ALMA in the 2 and 3 mm bands, aiming to determine a precise, unambiguous redshift via detection of several CO lines, similarly to the successful redshift determinations obtained by Weiß et al. (2009, 2013), Cox et al. (2011), Riechers et al. (2013), Asboth et al. (2016), Strandet et al. (2016), Oteo et al. (2016b), Fudamoto et al. (2017), or Riechers et al. (2017).

When our first deep 3 mm ALMA observations (see Section 2.2) were delivered, we found that the flux density at 870 μm (seen as extended emission in the LABOCA map of

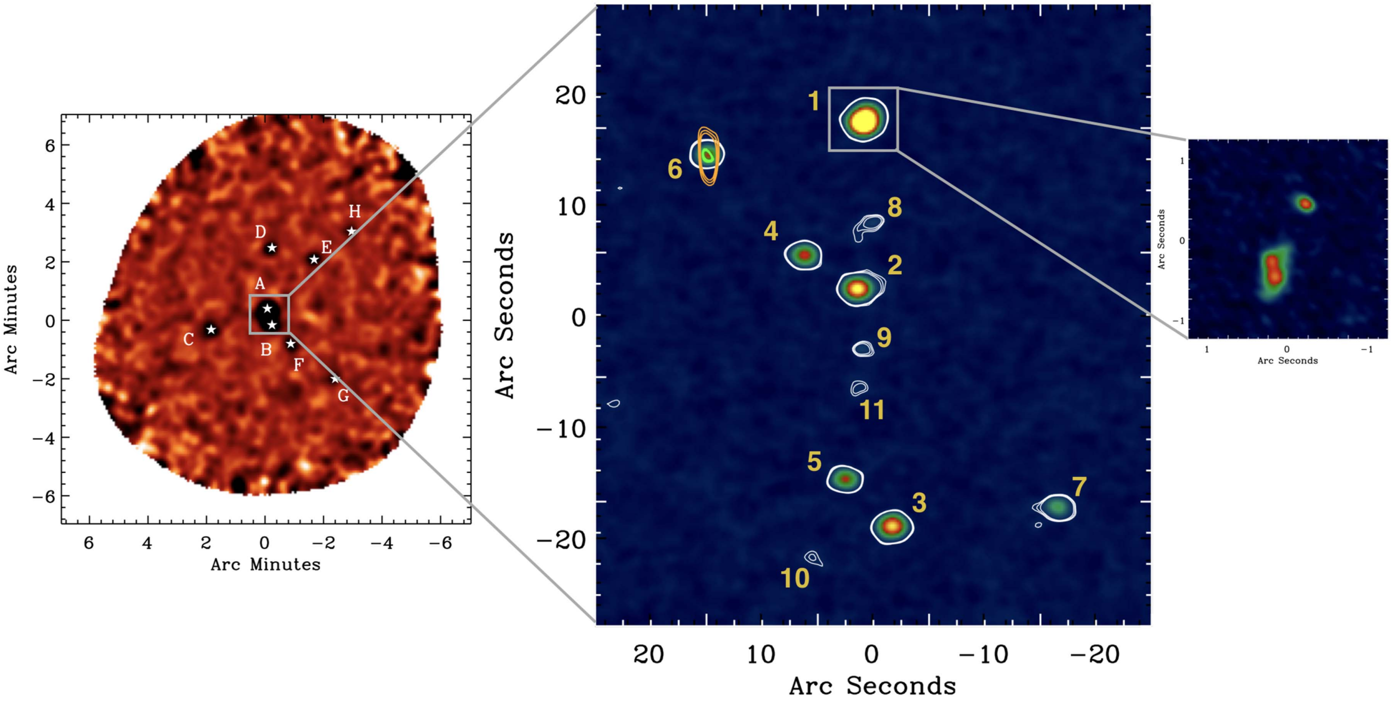

Figure 1. DRC from large to small scales—the core of an extreme protocluster of galaxies at $z_{\rm spec} = 4.002$. The left panel shows a wide-field LABOCA map at 870 μm of the environment of DRC, smoothed to a resolution of 27″. The eight DSFGs suggest an overdense field, because we would expect 2× times fewer sources (Lewis et al. 2017) according to the most recent single-dish submillimeter number counts (e.g., Geach et al. 2017). DRC is the extended LABOCA source associated with the DSFGs labeled A and B. The DSFGs around DRC (labeled C–H) all have $5 < S_{870\mu m}$ [mJy] < 11 and if all of them lie at the same redshift as DRC, then the collective obscured SFR would be ~14,400 $M_\odot$ yr^{-1}. This is considerably higher than any other starbursting structure at $z \gtrsim 4$ reported to date. The middle panel shows the ultra-deep ALMA 2 mm continuum map of DRC. Green and orange contours (from 5σ) represent the radio continuum emission observed by the Jansky VLA and ATCA, respectively. DRC is resolved into at least 11 components, which is also a significant overdensity of DSFGs according to the most recent ALMA number counts (Aravena et al. 2016; Oteo et al. 2016a; Dunlop et al. 2017). The right panel shows a high-resolution ALMA continuum map at 870 μm of the brightest DSFG in the protocluster, referred to here as DRC-1. This component is resolved into at least three star-forming clumps, whose interactions likely produce the extremely broad [C I](1–0) and ^{12}CO(6–5) line profiles (see Figure 2).

Table 1
Properties of DRC Components

Component	R.A.	Decl.	$S_{2\,\rm mm}$ (mJy)	$S_{3\,\rm mm}$ (mJy)	$v_{\rm center}$[a] (km s^{-1})	$L_{\rm IR}$ ($\times 10^{11}\,L_\odot$)	SFR[b] ($M_\odot$ yr^{-1})	$M_{\rm H_2}$[c] ($\times 10^{11}\,M_\odot$)	$\tau_{\rm dep}$ (Myr)
DRC–1	00:42:23.52	−33:43:23.4	2.117 ± 0.058	0.406 ± 0.028	−58 ± 32	161.5	~2900	~2.62	~90
DRC–2	00:42:23.56	−33:43:38.5	0.723 ± 0.011	0.154 ± 0.010	470 ± 97	55.2	~990	~1.18	~120
DRC–3	00:42:23.31	−33:43:59.9	0.659 ± 0.010	0.218 ± 0.022	286 ± 12	50.9	~902	~1.78	~200
DRC–4	00:42:23.95	−33:43:35.4	0.347 ± 0.099	0.075 ± 0.017	495 ± 27	26.5	~475	~1.08	~230
DRC–5	00:42:23.65	−33:43:55.7	0.295 ± 0.094	0.110 ± 0.012	…	22.5	~404	…	…
DRC–6	00:42:24.64	−33:43:26.4	0.282 ± 0.065	0.102 ± 0.011	−77 ± 26	21.5	~386	…	…
DRC–7	00:42:22.12	−33:43:58.2	0.176 ± 0.082	…	2010 ± 261	13.4	~241	…	…
DRC–8	00:42:23.46	−33:43:32.5	0.055 ± 0.010	…	−401 ± 38	4.2	~75	…	…
DRC–9	00:42:23.56	−33.43.47.3	0.042 ± 0.011	…	289 ± 17	3.2	~57	…	…
DRC–10	00:42:23.53	−33:43:43.9	0.040 ± 0.007	…	1643 ± 32	3.1	~55	…	…
DRC–11	00:42:23.87	−33.44.02.9	0.039 ± 0.009	…	492 ± 35	3.0	~53	…	…

Notes.

[a] Velocity center of the ^{12}CO(6–5) emission derived from a Gaussian fit to the line profile. These are Hubble flow velocities in the reference frame of an object at $z = 4.002$, assuming no peculiar velocities.

[b] SFRs have been obtained by rescaling the ALESS template to the observed 2 mm photometry of the DRC components. If the Arp 220 template had been used, the derived SFR would be higher than those presented in this table by a factor of ×1.4.

[c] In this work, we only report the molecular gas mass for those components detected in [C I](1–0); the molecular gas mass derived from ^{12}CO(6–5) would be highly uncertain due to the need to assume the shape of the CO spectral-line energy distribution (SLED) and the $\alpha_{\rm CO}$ conversion factor (see Ivison et al. 2011).

the source, see the left panel of Figure 1) was caused by an accumulation of bright DSFGs at $z = 3$–5 instead of being associated to a single source or merging system at very high redshift.

The ultra-deep ALMA continuum map at 2 mm reveals that the extended LABOCA source associated with DRC is resolved into at least 11 DSFGs (see the middle panel of Figure 1). Six of these components are also detected in the deep continuum map at 3 mm, while the other five are not detected due to the poorer sensitivity to dust emission at 3 mm. The main properties of DRC components, including their coordinates, velocities with respect to $z_{\rm spec} = 4.002$, SFRs, or molecular gas masses (whenever these are available) are shown in Table 1.

The number of sources in the ultra-deep ALMA continuum map at 2 mm represents a significant overdensity of DSFGs when compared with the most recent ALMA counts (Aravena et al. 2016; Oteo et al. 2016a; Dunlop et al. 2017) because only 1-2 DSFGs brighter than the faintest DRC component would be expected, and we have 11 of them. For this calculation, we have converted the 2 mm flux densities of DRC components into flux densities at 1.2 mm by using the ALESS template (Swinbank et al. 2014), which represents the average FIR SED of the classical DSFG population at $z \sim 2.5$ and has been found to provide a good representation of the FIR SED of ultrared DSFGs (Ivison et al. 2016). This number of components represents a lower limit if we consider that some of the individual 2 mm sources might be resolved into several components if they were observed at higher spatial resolution. This is what happens for DRC-1, the brightest component of the protocluster. Our high-resolution ALMA imaging at 870 μm reveals that this source is resolved into at least three bright star-forming clumps with extreme SFR densities of $\Sigma_{\rm SFR} \sim 800\text{–}2000\, M_\odot\ {\rm yr}^{-1}\,{\rm kpc}^{-2}$ (Oteo et al. 2017b), which is among the highest known (Riechers et al. 2014, 2017; Iono et al. 2016; Oteo et al. 2017a).

The spectral cubes associated with our ALMA 2 mm and 3 mm observations confirm that at least 10 of these components are at the same redshift, $z_{\rm spec} = 4.002$, via detection of up to five emission lines (we show the ^{12}CO(6–5) detections in Figure 2, the [C I](1–0), and $H_2O(2_{11}\text{–}2_{02})$ detections in Figure 3, and the ^{12}CO(4–3) and ^{12}CO(2–1) moment-0 maps in Figure 4—see also Table 2). They are therefore physically related, belonging to the same, massive structure. We note that the velocity distribution might suggest the existence of two groups (see Section 4.4 for more details). The spectroscopically confirmed sources extend over an area of 260 kpc × 310 kpc. This area is smaller than expected for protoclusters at $z \sim 4$ according to simulations (Chiang et al. 2013; Muldrew et al. 2015), but relatively close to the expected size of protocluster cores at $z = 4$ (Chiang et al. 2017). We thus consider it possible that DRC is the core of a larger protocluster structure to which at least some of the LABOCA-detected DSFGs around DRC (labeled from C to H in the left panel of Figure 1) might belong to. This needs to be confirmed with future spectroscopic observations. The possibility that some of the LABOCA sources around DRC might belong to the same structure suggests that despite the fact that star formation might be enhanced in the core (Shimakawa et al. 2017a), intense star formation might also be taking place across the full extension of the protocluster.

To establish a comparison, the protocluster SSA22 at $z = 3.09$ has eight spectroscopically confirmed DSFGs over an area of 0.7 Mpc × 1.4 Mpc (Umehata et al. 2015), while DRC has six spectroscopically confirmed DSFGs (considering only the sources within the same SFR range) over only 260 kpc × 310 kpc, and thus represents a much more overdense environment (with DRC having a 10× times higher source density) in terms of the dusty galaxy population. The same is true of other protocluster candidates, whose dusty components are distributed over much larger areas than those in DRC (e.g., Clements et al. 2016; Flores-Cacho et al. 2016).

Our deep Jansky VLA and ATCA observations revealed continuum emission from DRC-6 (see Figure 1) from 28 to 5.5 GHz ($S_{\rm 28\,GHz} = 96 \pm 15\ \mu$Jy, $S_{\rm 9.0\,GHz} = 120 \pm 8\ \mu$Jy, and $S_{\rm 5.5\,GHz} = 128 \pm 6\ \mu$Jy). For a DSFG, its radio spectrum is relatively flat (e.g., Ibar et al. 2010; Murphy et al. 2017). Furthermore, the low FIR-to-radio flux density ratio in this component—the radio emission is ~50× brighter than would be predicted from the ALESS template (Swinbank et al. 2014) used in several discussions in this paper—suggests the presence of an AGN (Guidetti et al. 2017). No radio emission was detected in any of the other DRC components, which could suggest that the radio-loud phase is shorter than the starburst phase. Alternatively, several DRC components could be in a radio-loud phase, hidden from us because their jets are misaligned with our line of sight. Either way, our radio observations reveal at least one AGN, and thus presumably a black hole that is growing while its host galaxy forms stars.

The existence of a significant overdensity of luminous DSFGs at $z_{\rm spec} = 4.002$ over a 260 kpc × 310 kpc area supports the idea that, at least in some cases, bright DSFGs trace dense environments, which agrees with several previous findings (e.g., Stevens et al. 2003; Venemans et al. 2007; Tamura et al. 2009; Ivison et al. 2013; Dannerbauer et al. 2014; Umehata et al. 2014, 2015; Casey et al. 2015; Wang et al. 2016).

The nature of DRC was established by following up with ALMA on a sample of ultrared DSFGs, which were initially selected because of their red SPIRE colors, as confirmed by ground-based imaging observations at 850 or 870 μm using SCUBA-2 and/or LABOCA, data which improved the accuracy of photometric redshift estimates (Ivison et al. 2016). These ultrared DSFGs were distributed over all the *H*-ATLAS fields, a total sky area of ~600 deg^2. The fact that this is the first extreme protocluster in *H*-ATLAS suggests the number density of such structures is $N\,[{\rm deg}^{-2}] \gtrsim 1.7 \times 10^{-3}$. Note that this is the number density of protoclusters, not sources within protoclusters. Recently, Negrello et al. (2017) presented the expected number of protoclusters as a function of their total $L_{\rm IR}$ and redshift, using the galaxy evolution models of Cai et al. (2013). At $z > 4$, Negrello et al. (2017) predicted $N\,[{\rm deg}^{-2}] > 10^{-2}$ protoclusters with $L_{\rm IR} \sim 3.7 \times 10^{13}\, L_\odot$, the total IR luminosity of DRC. These predictions are consistent with DRC because (1) we can only derive a lower limit on the number of luminous protoclusters since we have not followed up with ALMA all ultrared DSFGs in *H*-ATLAS, and (2) we have only imaged the central part of the protocluster; if some of the LABOCA sources around DRC belong to the same structure, then $L_{\rm IR}$ may increase considerably.

3.1. Redshift Confirmation of DRC: the Full Story

As an example of the difficulties sometimes encountered when trying to confirm redshifts via the detection of atomic and/or molecular lines in submillimeter and millimeter windows, it is worth mentioning that the redshift of DRC was only confirmed unambiguously after a large series of observations spanning several years. First, DRC was included in the sample of ultrared galaxies from the *H*-ATLAS survey (Ivison et al. 2016; Fudamoto et al. 2017) selected for spectral scans in the 3 mm band with ALMA. In those spectral scans of DRC, we detected only very faint emission in the center of the

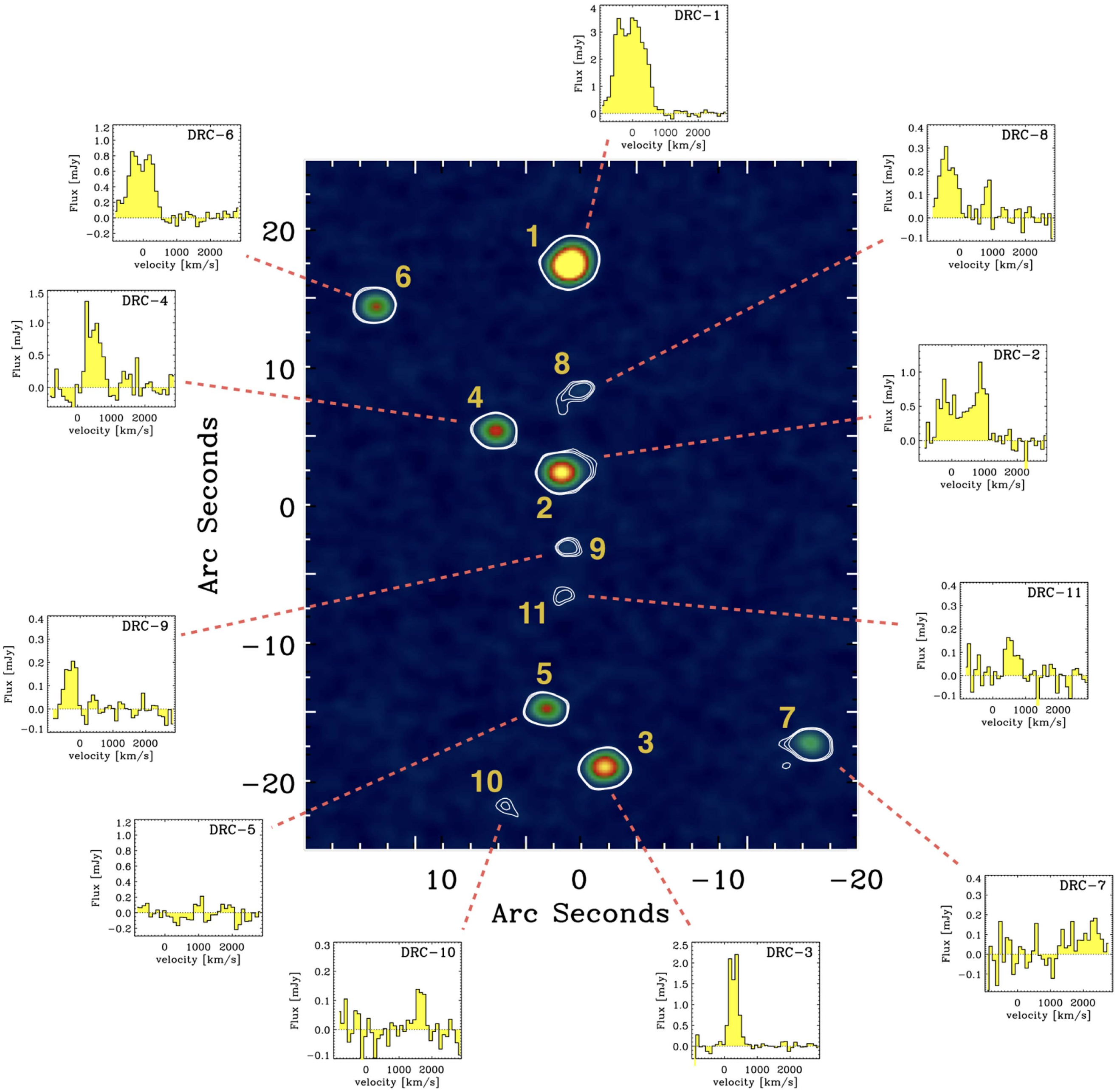

Figure 2. Spectroscopic confirmation of the protocluster members at $z_{\rm spec} = 4.002$ via detection of ^{12}CO(6–5) emission (additional [C I](1–0), $H_2O(2_{11}–2_{02})$, ^{12}CO(4–3) and ^{12}CO(2–1) detections are shown in Figures 3–5). We have considered that the redshift of the structure corresponds to the redshift of DRC-1, its brightest component. The central panel shows the same 2 mm ultra-deep continuum imaging already shown in the central panel of Figure 1. The ^{12}CO(6–5) detections confirm that at least 10 of the 11 continuum sources belong to the protocluster. The lack of ^{12}CO(6–5) emission in DRC-5 does not necessarily mean that it does not belong to the protocluster, because the spectral setup of our ALMA observations does not cover velocities, $v < -1000$ km s^{-1}. There is a wide range of line profiles, from relatively narrow emission (DRC-10) to extremely broad lines, as wide as ~1000 km s^{-1} (DRC-1) or ~2100 km s^{-1} (DRC-2). Note that the horizontal axes are not centered at $v = 0$ km s^{-1} because the spectral setup of the ALMA observations only covers $v > -1000$ km s^{-1}.

band, which was interpreted at ^{12}CO(7–6) alongside C I(2–1). DRC was then observed through an ALMA DDT program to confirm these lines. However, the observations revealed a single, extremely broad emission line that we initially associated with CO, which then yielded several discrete possibilities for the redshift. We checked three different redshift options using the Jansky VLA, but no CO line was detected. Our ALMA Cycle 4 observations, aimed at confirming the redshift of DRC unambiguously, finally detected a second and a third emission line, neither were at the frequency we were expecting. These detections, of what could only be ^{12}CO(6–5) and $H_2O(2_{11}–2_{02})$, revealed that the initial line detected in the ALMA 3 mm and DDT observations was not CO, but instead [C I](1–0), and that the redshift of DRC is $z_{\rm spec} = 4.002$. At this redshift, the ^{12}CO(4–3) transition was covered by our 3 mm spectral scan, but in a noisy region that prevented the line profile from being detected. It should also be noted that because DRC lies close to the edge of the *H*-ATLAS image of the South Galactic Pole, it sometimes dropped out of the *H*-ATLAS catalogs, depending on how much padding was adopted, leading to some confusion.

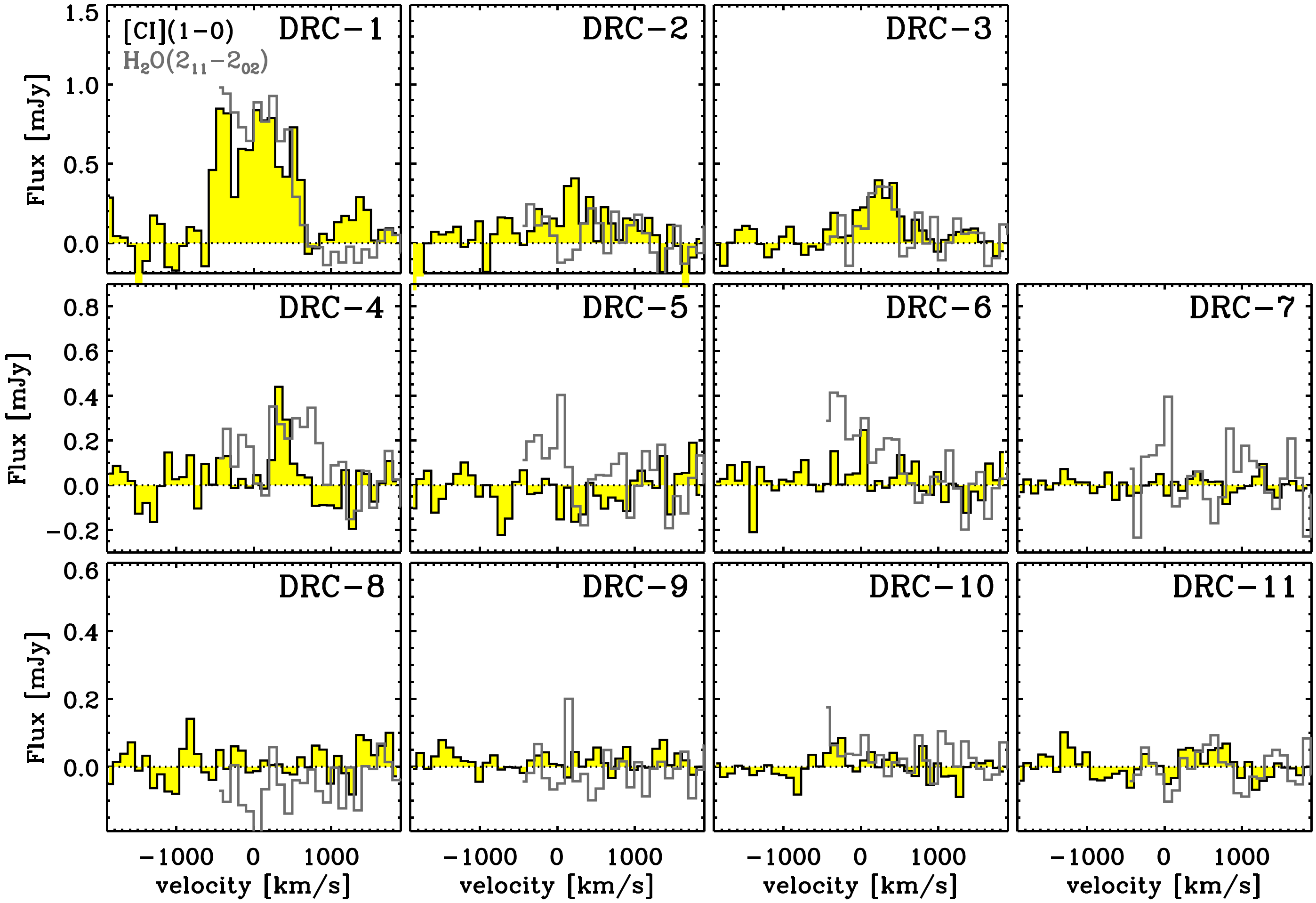

Figure 3. ALMA continuum-subtracted [C I](1–0) and $H_2O(2_{11}–2_{02})$ spectra of the 11 components in the core of our extreme protocluster, DRC, at $z_{spec} = 4.002$. The detection of these two additional emission lines in some DRC components provides unambiguous confirmation of the redshift. Note that only about half of the line profile of the water emission has been detected in most of the DRC components. This is because the spectral setup of the 2 mm observations was defined assuming that the emission line seen in our previous 3 mm observations was CO; it was actually [C I](1–0), so we did expect to cover the water transition.

4. Properties of DRC

4.1. Total Star Formation Rate

In order to estimate the total SFR of the 10 spectroscopically confirmed DRC components (see Table 1), we use their observed flux densities at 2 mm, corresponding to ∼400 μm in the rest frame, which is the only wavelength where the continuum emission from all the DRC components has been detected. The flux density at 2 mm of each DRC component is converted to an SFR (see values for individual components in Table 1) by rescaling the ALESS template and integrating it between rest-frames 8 and 1000 μm. This method assumes that the SEDs (from 8 to 1000 μm in the rest frame) of all DRC components are well represented by the ALESS template, a fact that should be considered when comparing DRC to other protoclusters. Under the same assumption, the continuum sensitivity of our ALMA 2 mm observations indicates that we are sensitive to sources with SFR $\gtrsim 40\,M_\odot\,\mathrm{yr}^{-1}\,(3\sigma)$. We include DRC-5 in Table 1, assuming that it belongs to the same protocluster structure, although no emission line has been detected from this component. This is because our observations only covered $v > -1000\,\mathrm{km\,s}^{-1}$ and, consequently, we cannot be sure that DRC-5 does not belong to the protocluster.

Among the SED templates used in Ivison et al. (2016), which include a representative range, only the one reported by Pearson et al. (2013) yields lower SFRs than the ALESS SED template, by a factor of 0.66×. The Cosmic Eyelash SED (Ivison et al. 2010; Swinbank et al. 2010) and the SED template reported by Pope et al. (2008) yield similar SFRs to the ALESS template. The Arp 220 SED gives higher SFRs than the ALESS template by a factor of 1.36×. The same happens for the SED of the lensed source, G15.141 at $z = 4.24$ (Cox et al. 2011; Lapi et al. 2011), which yields SFRs higher than the ALESS template by a factor of 2.21×. Therefore, although the uncertainties can be significant, the SED template used in this work to measure SFRs does not give the highest SFR—we are being conservative (modulo the possibility of a profoundly different IMF in these objects—Romano et al. 2017). Therefore, the high SFRs measured for the DRC components are not artificially high because of the chosen template, but because they are truly luminous.

The total obscured SFR of DRC—which, recall, is only the core of our larger overdensity of DSFGs—is as extreme as SFR $\sim 6500\,M_\odot\,\mathrm{yr}^{-1}$, and about 75% of that is taking place in three DRC components: DRC-1, DRC-2, and DRC-3, those with $L_{\rm IR} \geqslant 5 \times 10^{12}\,L_\odot$. The obscured SFR of the protocluster core derived from the ALMA continuum emission at 2 mm is lower in a factor of 1.37× than that derived from the flux density associated with its extended LABOCA 870 μm emission (components A and B in the left panel of

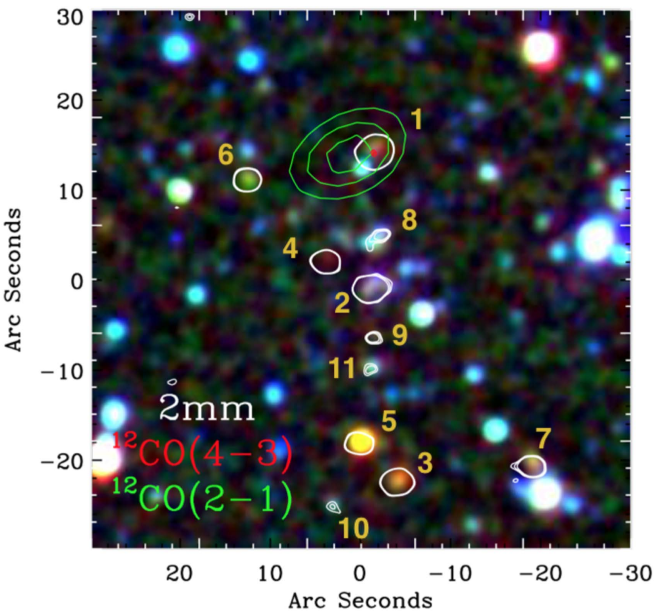

Figure 4. False-color image of the core of our protocluster at $z_{\rm spec} = 4.002$, obtained from our I-, K_S-band and IRAC imaging. The positions of the 11 DRC components are highlighted by white contours; ^{12}CO(2–1) emission from ATCA is shown with green contours and the ALMA ^{12}CO(4–3) emission is shown with red contours (note that this faint emission is on top of DRC-1). All contours run from 4σ to 6σ in steps of 1σ. Most DRC components are detected in at least one optical/near-IR band and a variety of colors is seen, with the brightest sources at 2 mm having the reddest optical/near-IR colors.

Table 2
Line Properties of DRC Components

Component	$I_{\rm [C\,I](1-0)}$ (mJy km s^{-1})	$I_{\rm ^{12}CO(6-5)}$ (mJy km s^{-1})	FWHM $_{\rm ^{12}CO(6-5)}$[a] (km s^{-1})
DRC–1	882 ± 119	4192 ± 331	1009 ± 88
DRC–2	394 ± 54	1748 ± 337	2140 ± 466
DRC–3	598 ± 76	757 ± 64	359 ± 29
DRC–4	364 ± 44	539 ± 56	602 ± 68
DRC–5	…	…	…
DRC–6	…	767 ± 58	840 ± 70
DRC–7	…	169 ± 53	1296 ± 472
DRC–8	…	130 ± 24	515 ± 104
DRC–9	…	109 ± 18	380 ± 70
DRC–10	…	52 ± 14	288 ± 85
DRC–11	…	33 ± 11	243 ± 89

Note.
[a] Obtained from Gaussian fits to the line profiles. Note that the ^{12}CO(6–5) emission in DRC-2 has a very high linewidth because of the boxy shape of the line profile. In any case, the FWZI of the ^{12}CO(6–5) emission in DRC-2 is ∼1600 km s^{-1}.

Figure 1), $S_{870\mu\rm m} = 64 \pm 11$ mJy, which would imply SFR $\sim 8900\,M_\odot$ yr^{-1}. It is also lower in a 1.34× factor than the obscured SFR associated to the total IR luminosity derived in Ivison et al. (2016) from the *Herschel*+LABOCA/SCUBA-2 photometry. One reason for this discrepancy could be that the ALESS SED template does not provide a good representation of the dust emission for all the DRC components, such that some of them would have higher SFRs than those reported in Table 1.

The total obscured SFR of our protocluster core is the highest reported so far for protoclusters whose members have been spectroscopically confirmed at $z > 4$. As a reference, the total obscured SFR of AzTEC-3, a massive protocluster at $z_{\rm spec} = 5.3$ (Capak et al. 2011), is SFR $\sim 1600\,M_\odot$ yr^{-1} as estimated from the only DSFG in this system. For a comparison at slightly lower redshifts, the total obscured SFR in the core of the protocluster SSA22 at $z_{\rm spec} = 3.09$ (Steidel et al. 1998; Yamada et al. 2012) is SFR $\sim 3,820\,M_\odot$ yr^{-1}, calculated from the observed flux density at 1.1 mm of the components and adopting the ALESS SED template, as with DRC). CL J001, a concentration of DSFGs at $z_{\rm spec} = 2.5$ (Wang et al. 2016) has SFR $\sim 3400\,M_\odot$ yr^{-1} in the central 80 kpc region, much lower than DRC. One of the few comparable cases in terms of the high obscured SFR is the COSMOS protocluster at $z = 2.10$ reported by Yuan et al. (2014) and Hung et al. (2016), but its SFR was determined over much wider scales than the core of our protocluster and, additionally, the COSMOS structure is at much lower redshift than DRC.

As reported above, DRC is just the core of an overdensity of DSFGs. The total 870 μm of all these DSFGs (the eight LABOCA sources, including DRC—see left panel of Figure 1) is ≈106 mJy. If all those DSFGs were at the same redshift as DRC, the total SFR of the system would be around 14,400 $M_\odot$ yr^{-1}. The fact that the DSFGs found around DRC are at its same redshift is supported by their photometric redshifts measured from the *Herschel* plus LABOCA/SCUBA-2 photometry (Lewis et al. 2017), although further observations are required to confirm this.

4.2. Molecular Gas Mass

The [C I](1–0) transition has been proposed to be a good tracer of the total molecular gas mass, even better than low-J CO lines in high-redshift galaxies (Papadopoulos et al. 2004) and it has been used to estimate the molecular gas of several populations of high-redshift DSFGs (e.g., Walter et al. 2011; Alaghband-Zadeh et al. 2013; Bothwell et al. 2017). In this work, we use [C I](1–0) to estimate the molecular gas mass for the DRC components detected in that transition (see Figure 3). The line fluxes have been derived from the moment-0 maps of [C I](1–0) for each component. For the DRC components whose [C I](1–0) line is not detected (see, for example, DRC-2, whose [C I](1–0) is not clearly detected in the spectrum—the line is expected to be extremely broad, judging by the ^{12}CO(6–5) profile), we have assumed that the [C I](1–0) and ^{12}CO(6–5) transitions have the same width. Then, we have calculated the H$_2$ mass of each DRC component following Bothwell et al. (2017) and Alaghband-Zadeh et al. (2013), but see also Papadopoulos & Greve (2004), Papadopoulos et al. (2004), and Weiß et al. (2003, 2005):

$$M_{\rm H_2} = 1375.8\, D_{\rm L}^2 (1+z)^{-1} \left(\frac{X_{\rm [C\,I]}}{10^{-5}}\right)^{-1} \times \left(\frac{A_{10}}{10^{-7}\ {\rm s}^{-1}}\right)^{-1} \times Q_{10}^{-1}\, S_{\rm [C\,I]}\, \Delta v, \qquad (1)$$

where $X_{\rm [C\,I]}$ is the [C I]/H$_2$ abundance ratio (assumed to be $X_{\rm [C\,I]} = 3 \times 10^{-5}$), A_{10} is the Einstein coefficient ($A_{10} = 7.93 \times 10^{-8}$ s^{-1}), and Q_{10} is the excitation factor, assumed to be $Q_{10} = 0.6$ (Bothwell et al. 2017). Equation (1) does not take into account the effect of the cosmic microwave background (CMB) on the [C I](1–0) line strength (da Cunha et al. 2013; Zhang et al. 2016). The CMB at $z = 4$ has a temperature of

$T_{\rm CMB} \sim 13.7$ K, which is not negligible compared to the upper level of the [C I](1–0) line, ∼23.6 K. In order to estimate the magnitude of the effect of the CMB, we take into account that the upper level of the [C I] line lies between the upper level energies of ^{12}CO(2–1) and ^{12}CO(3–2). Following da Cunha et al. (2013), the effect of the CMB would then be a suppression of the velocity-integrated flux of the [C I](1–0) line by a factor of ∼2×, assuming local thermodynamic equilibrium (the precise factor depends on the kinetic temperature). This means that the molecular gas masses of the DRC components would be a factor of 2× higher than those given by Equation (1). This a very crude estimation, since the effect of the CMB on the observed line fluxes depends on a number of factors. The molecular gas masses of the DRC components, derived with the above assumptions, are quoted in Table 1. It can be seen that our protocluster is formed by galaxies with massive molecular gas reservoirs, whose gas masses range from $M_{\rm H_2} \sim 1.1 \times 10^{11}\,M_\odot$ to $M_{\rm H_2} \sim 2.6 \times 10^{11}\,M_\odot$. The total molecular gas is at least $M_{\rm H_2} \sim 6.6 \times 10^{11}\,M_\odot$.

Our ALMA 3 mm scan also covered the ^{12}CO(4–3) emission line. It was not detected because of its faintness and because the noise was higher near its frequency. Once the redshift of DRC was confirmed, we calculated the moment-0 map of the ^{12}CO(4–3) emission, assuming that it is as wide as the ^{12}CO(6–5) transition detected in our ALMA band 4 observations. ^{12}CO(4–3) emission is detected in the moment-0 map only from DRC-1. Using this line flux to measure the molecular gas mass of this DRC component, assuming the average luminosity ratio of CO lines in DSFGs, $L'_{\rm CO(4-3)}/L'_{\rm CO(1-0)} = 0.46$ (Ivison et al. 2011; Bothwell et al. 2013; Carilli & Walter 2013) and the $\alpha_{\rm CO}$ for local ULIRGs, $\alpha_{\rm CO} = 0.8 M_\odot ({\rm K\ km\ s^{-1}\ pc^2})^{-1}$ (Downes & Solomon 1998), the derived molecular gas mass for DRC-1 from ^{12}CO(4–3) is $M_{\rm H_2} \sim 1.1 \times 10^{11}\,M_\odot$. This value is lower than the molecular gas mass of DRC-1 derived from [C I](1–0), but is consistent given the large uncertainties involved in such determinations.

The molecular gas mass for the other DRC components could be determined from the detected ^{12}CO(6–5) line transitions. However, this would lead to a very uncertain estimates because of the conversion from ^{12}CO(6–5) to ^{12}CO(1–0) luminosity and the conversion from ^{12}CO(1–0) luminosity to molecular gas mass. Alternatively, we could use the rest-frame 870 μm luminosity as a proxy for the molecular gas mass, following Scoville et al. (2016), Hughes et al. (2017), and Oteo et al. (2017c). For the DRC components with [C I](1–0) detections, the molecular gas masses derived from [C I](1–0) are ∼2–5× lower than those derived from the dust continuum luminosity, where the rest-frame luminosities at 870 μm have been obtained by redshifting the ALESS template to $z = 4.002$ and rescaling to the observed flux density of each DRC component at 2 mm. We report only the molecular gas mass of the sources detected in [C I](1–0), noting that the total molecular gas mass of our protocluster might be much higher (also considering that some of the LABOCA-detected DSFGs around DRC might be at the same redshift).

4.3. Gas-depletion Time

We can estimate the gas-depletion time of the DRC components detected in [C I](1–0) from the ratio between their molecular gas masses and their SFRs. These are shown in Table 1 and range between ∼90 and 230 Myr. These gas-depletion times are comparable to those obtained for other luminous DSFGs at $z \gtrsim 4$ (Riechers et al. 2013, 2017; Hodge et al. 2015; Oteo et al. 2016b; Fudamoto et al. 2017).

The probability of detecting 10 short-lived, physically associated DSFGs—we do not consider DRC-5 here due to the lack of spectroscopic confirmation—is extremely low (see, for example, Casey 2016), meaning that such structures are extraordinary systems. The fact that some DRC components are detectable as luminous DSFGs at the same redshift and with relatively low gas-depletion times might suggest the existence of a mechanism that is able to trigger star formation simultaneously in different sources distributed across hundreds of kiloparsecs. Alternatively, given that the baryon to dark-matter ratio in galaxies is much lower than the cosmic value, such that halos contain huge amounts of gas that can flow to the star-forming regions, one can argue that star formation can be sustained over longer times until it is swept out by feedback effects; though, the absence of "normal" SFGs is puzzling. Relatively long starburst lifetimes have been reported in the past (Granato et al. 2004; Lapi et al. 2011), while others have reported the presence of galaxies in high-redshift clusters whose scatter in age is only a few hundreds megayears (Andreon et al. 2014).

4.4. Velocity Dispersion and Total Mass

Using the ^{12}CO(6–5) line detections, which provide the highest signal-to-noise among all the detected lines, we have measured the central velocity of all the DRC components (see Table 1), from which we can derive a velocity dispersion, $\sigma_{\rm v} = 794\ {\rm km\ s^{-1}}$. This relatively high velocity dispersion is mainly caused by the velocity of components DRC-7 and DRC-10 with respect to the others. The fact that these two components have velocity offsets as large as ∼2000 km s^{-1} with respect to the average velocity of all the other components might mean that we are seeing two groups, as has been reported in protoclusters at lower redshifts such as MRC 0052-241 at $z = 2.86$ (Venemans et al. 2007). We note that the velocity dispersion has been obtained from only 10 spectroscopically confirmed sources in the core of the protocluster.

We can estimate the total mass of our protocluster using several different methods. First, we can use the velocity dispersion ($\sigma_{\rm v}$) and the relation between the velocity dispersion and the total mass ($M_{\rm total}$) derived by Evrard et al. (2008), which has also been used to estimate the total mass of lower-redshift protoclusters (Wang et al. 2016):

$$\sigma_{\rm v}(M, z) = \sigma_{\rm DM,15}\left(\frac{h(z)M_{\rm total}}{10^{15}\,M_\odot}\right)^{\alpha}, \qquad (2)$$

where $h(z)$ is the dimensionless Hubble parameter. Using $\sigma_{\rm DM,15} \sim 1,083\ {\rm km\ s^{-1}}$, and $\alpha \sim 0.336$ (see also Wang et al. 2016), we derive a total mass of $M_{\rm total} \sim 9.3 \times 10^{13}\,M_\odot$. We note that this estimate is highly uncertain for two main reasons. First, protoclusters at $z \sim 4$ are not virialized. Second, the velocity dispersion has been measured using only the spectroscopically confirmed sources, which are all located in the core (the most violent region, which is forming stars at a rate of thousands of $M_\odot\ {\rm yr^{-1}}$). We can also estimate the total mass of the cluster by assuming a uniform spherical distribution with line-of-sight velocity dispersion and radius corresponding to those for our protocluster core. In this case, the virial mass would be $M_{\rm total} \sim 3.2 \times 10^{13}\,M_\odot$, slightly lower than the previous estimate. Next, we estimate the total mass using the relation between the total IR luminosity and halo mass at $z = 4$ by Aversa et al. (2015), obtaining $M_{\rm total} \sim 4.4 \times 10^{13}\,M_\odot$.

The different methods used above to estimate the total mass of the protocluster core give a wide range of values, indicative of the uncertain nature of this task. Despite the uncertainties, we have determined that our protocluster core is very massive. The total mass of the full protocluster would be considerably higher still, considering that DRC is only the core. It could be even more massive than the most massive progenitor halos predicted by simulations. As a reference, Chiang et al. (2013) predicted $<2 \times 10^{13}\,M_\odot$ at $z = 4$. Using the evolutionary tracks of Chiang et al. (2013), we conclude that DRC might become an ultra-massive cluster at $z = 0$, with a total mass in the region of $2 \times 10^{15}\,M_\odot$; thus, DRC could be the progenitor of a Coma-like (The & White 1986; Kubo et al. 2007) or even more massive cluster. However, we note that exploring the evolution of DRC is highly uncertain because we are only probing the core of a likely larger overdensity of DSFGs and halos with similar masses can evolve very differently. Further observations of the surroundings of DRC would be needed to have a better insight of the evolution (i.e., if DRC is truly the progenitor of a massive galaxy cluster or it is just a group of sources caught in a active stage during their evolution) of this extreme structure we have discovered.

4.5. Stellar and Lyα Emission

Figure 4 shows a false-color image of the stellar emission in the components of our protocluster core, which has been created using R, K_s, and IRAC 4.5 μm imaging. A variety of colors can be seen, with the brightest components at 2 mm being associated to reddest sources, as expected. We note that our optical and near-IR imaging does not reveal any sign (like arcs), which might indicate that our protocluster is being gravitationally amplified by a foreground cluster.

Using our MUSE observations of the protocluster core, we have created a continuum-subtracted Lyα image, which is shown in the top panel of Figure 5. The Lyα image reveals the presence of a Lyα blob next to DRC-2 that extends over 60 kpc; similar to what is found around other high-redshift DSFGs (Ivison et al. 1998; Chapman et al. 2001; Umehata et al. 2015; Geach et al. 2016; Cai et al. 2017) and radio galaxies (Swinbank et al. 2015). Actually, as discussed in Chiang et al. (2015), there is a tendency for there to be extended Lyα emission in overdense environments (Matsuda et al. 2009; Yang et al. 2009; Erb et al. 2011; Matsuda et al. 2012). We note that part of the emission in this Lyα blob might be contaminated by a spectroscopically confirmed [O II] emitter located at the south the Lyα blob (there is an additional [O II] emission northwest of the MUSE field. The lower panel of Figure 5 shows the spectrum of the Lyα blob, integrated over its full extent, in comparison to the ^{12}CO(6–5) line profile of the DRC component right next to it. The Lyα emission is even wider than the ^{12}CO(6–5), but is still comparable to other Lyα blobs at these redshifts.

It can be seen in Figure 4 that most of the DRC components detected at CO and 2 mm continuum do not show significant Lyα emission, as expected for DSFGs (although there are exceptions to this—Chapman et al. 2003, 2005; Casey et al. 2012; Oteo et al. 2012a, 2012b; Sandberg et al. 2015). Furthermore, apart from the Lyα blob, no Lyα emitters are found in the 1′ × 1′ central region of the protocluster (the emission-line galaxy detected in the northeast is a low-redshift [O II] emitter, with strong continuum and Balmer absorption lines), indicating that the star formation in this most extreme region is dominated by dust-obscured star formation. This might be a consequence of an extra Lyα depletion in the core

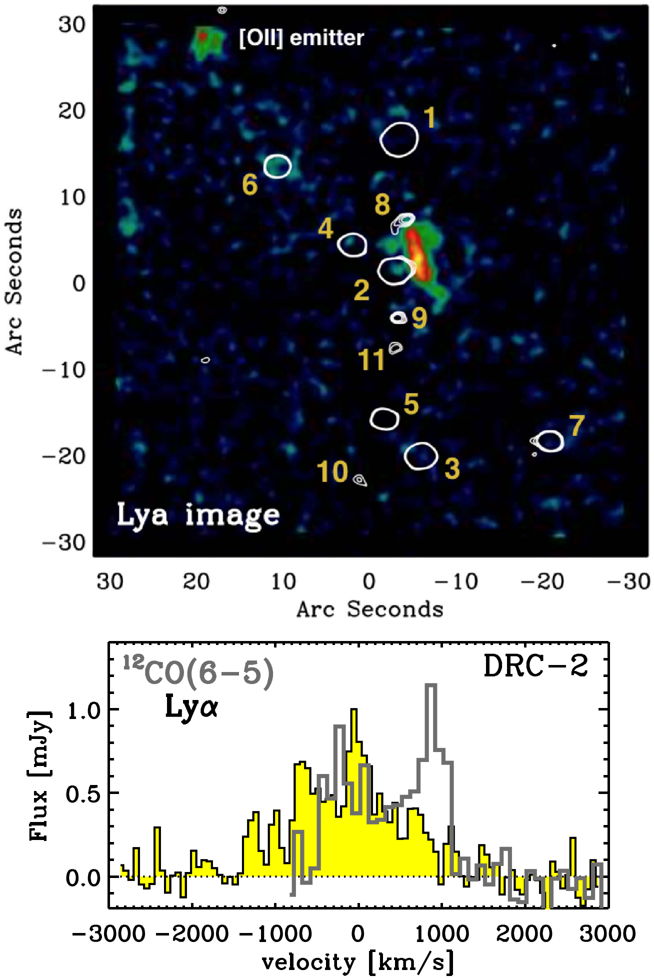

Figure 5. Top: Lyα image of the protocluster core, showing the Lyα blob next to DRC-2 (north is up; east is left), which extends over 60 kpc. Since the Lyα blob is faint, the image shown here has been smoothed using a 5 pixel × 5 pixel Gaussian kernel. The emission seen to the northeast is [O II] from a star-forming galaxy at low redshift ($z_{\rm spec} = 0.637$). The protocluster components are shown with white contours representing the 2 mm continuum emission, which run from 4σ to 6σ in steps of 1σ. Apart from the Lyα blob, no other Lyα emitter is detected in the field, indicating that the most extreme region of our protocluster is dominated by DSFGs and not by "normal" SFGs. We note that some of the flux of the Lyα blob might be affected by the [O II] emission of a low-redshift SFG located at the southern end of the blob. Bottom: Spectrum of the Lyα blob, compared to the ^{12}CO(6–5) emission in DRC-2. The flux scale corresponds to the ^{12}CO(6–5) transition, and the Lyα has been rescaled to fit. The Lyα blob profile is extremely broad (even broader than the ^{12}CO(6–5) emission), with an FWZI greater than 2,000 km s^{-1}. This value is comparable to those seen in Lyα blobs associated with radio galaxies at $z \sim 4$ (Swinbank et al. 2015).

of high-redshift protoclusters, as discussed in Shimakawa et al. (2017b).

5. Conclusions

In this paper, we have reported the identification of an extreme protocluster of DSFGs at $z_{\rm spec} = 4.002$ whose core (defined as the region where the SFR is maximal) is associated with one of the reddest sources in *H*-ATLAS (nicknamed DRC). It comprises at least 10 DSFGs, distributed over an area of 260 kpc × 310 kpc, with a total SFR of at least $6,500\,M_\odot\,{\rm yr}^{-1}$. Most of this SFR is taking place in the dusty DSFGs—our MUSE Lyα imaging reveals no *normal* star-forming galaxies in the protocluster core, just a 60 kpc wide Lyα blob next to one of the DRC components, and at the same redshift. The mass of the core of the protocluster is also extreme—at least $\sim 6.6 \times 10^{11}\,M_\odot$, just in molecular gas.

DRC is the brightest component of an overdensity of DSFGs discovered in an LABOCA wide-field observation around the protocluster core. If all these additional DSFGs were at the same redshift as DRC—meaning the total SFR would be $\sim 14,400\,M_\odot\,{\rm yr}^{-1}$—the structure would have an extent of at least 2.3 Mpc × 2.3 Mpc, close to the expected size of protoclusters at $z \sim 4$ according to simulations, although the progenitors of the most massive clusters in the local universe can extend across ∼15 Mpc in diameter at the redshift of DRC (Chiang et al. 2013).

The core of the protocluster has a molecular gas mass of at least $6.6 \times 10^{11}\,M_\odot$ and its total mass could be as high as $\sim 4.4 \times 10^{13}\,M_\odot$. This is slightly more massive than models predict for the most massive progenitor halos and could suggest that DRC may evolve into a cluster at $z = 0$ with a total mass $> 10^{15}\,M_\odot$ and, therefore, could be the early progenitor of a cluster at least as massive as Coma.

The gas-depletion times of those DRC components with reliable molecular gas mass determinations are relatively low, ranging between 90 and 230 Myr. This suggests either the presence of an unknown mechanism, able to trigger extreme star formation almost simultaneously in sources distributed over a few hundred kiloparsec scales in the early universe, or alternatively the presence of gas flows from the cosmic web, able to sustain star formation over much longer times than the estimated gas-depletion times.

I.O., R.J.I., L.D., S.M., Z.-Y.Z., and A.J.R.L. acknowledge support from the European Research Council (ERC) in the form of Advanced Grant, COSMICISM. I.O. acknowledges G. Bendo and M. Zwaan for their help with the ALMA data calibration and analysis. L.D. also acknowledges support from ERC Consolidator Grant, CosmicDust. D.R. acknowledges support from the National Science Foundation under grant number AST-1614213. We would like to thank M. J. Michałowski, E. Valiante, Zheng Cai, Rhythm Shimakawa, and Stefano Andreon for their useful comments on the paper. This paper makes use of the following ALMA data: ADS/JAO.ALMA#2013.1.00449.S, ADS/JAO.ALMA#2013.A.00014.S, 2013.1.00001.S, and 2016.1.01287.S. ALMA is a partnership of ESO (representing its member states), NSF (USA) and NINS (Japan), together with NRC (Canada) and NSC and ASIAA (Taiwan) and KASI (Republic of Korea), in cooperation with the Republic of Chile. The Joint ALMA Observatory is operated by ESO, AUI/NRAO, and NAOJ. The National Radio Astronomy Observatory is a facility of the National Science Foundation operated under cooperative agreement by Associated Universities, Inc. Based on observations made with ESO Telescopes at the La Silla Paranal Observatory under programs ID 295.A-5029 and ID 093.A-0705. The Australia Telescope Compact Array is part of the Australia Telescope National Facility, which is funded by the Australian Government for operation as a National Facility managed by CSIRO. Based on observations obtained at the Gemini Observatory, which is operated by the Association of Universities for Research in Astronomy, Inc., under a cooperative agreement with the NSF on behalf of the Gemini partnership: the National Science Foundation (United States), the National Research Council (Canada), CONICYT (Chile), Ministerio de Ciencia, Tecnología e Innovación Productiva (Argentina), and Ministério da Ciência, Tecnologia e Inovação (Brazil). This work is based [in part] on observations made with the *Spitzer Space Telescope*, which is operated by the Jet Propulsion Laboratory, California Institute of Technology under a contract with NASA.

ORCID iDs

I. Oteo https://orcid.org/0000-0001-5875-3388

References

Alaghband-Zadeh, S., Chapman, S. C., Swinbank, A. M., et al. 2013, MNRAS, 435, 1493
Allen, S. W., Evrard, A. E., & Mantz, A. B. 2011, ARA&A, 49, 409
Andreon, S., Newman, A. B., Trinchieri, G., et al. 2014, A&A, 565, A120
Aravena, M., Decarli, R., Walter, F., et al. 2016, ApJ, 833, 68
Asboth, V., Conley, A., Sayers, J., et al. 2016, MNRAS, 462, 1989
Aversa, R., Lapi, A., de Zotti, G., Shankar, F., & Danese, L. 2015, ApJ, 810, 74
Bacon, R., Accardo, M., Adjali, L., et al. 2010, Proc. SPIE, 7735, 773508
Bacon, R., Brinchmann, J., Richard, J., et al. 2015, A&A, 575, A75
Bertin, E. 2010, SWarp: Resampling and Co-adding FITS Images Together, Astrophysics Source Code Library
Borgani, S., & Kravtsov, A. 2011, ASL, 4, 204
Bothwell, M. S., Aguirre, J. E., Aravena, M., et al. 2017, MNRAS, 466, 2825
Bothwell, M. S., Smail, I., Chapman, S. C., et al. 2013, MNRAS, 429, 3047
Bremer, M. N., Valtchanov, I., Willis, J., et al. 2006, MNRAS, 371, 1427
Cai, Z., Fan, X., Yang, Y., et al. 2017, ApJ, 837, 71
Cai, Z.-Y., Lapi, A., Xia, J-Q., et al. 2013, ApJ, 768, 21
Capak, P. L., Riechers, D., Scoville, N. Z., et al. 2011, Natur, 470, 233
Carilli, C. L., & Walter, F. 2013, ARA&A, 51, 105
Casey, C. M. 2016, ApJ, 824, 36
Casey, C. M., Berta, S., Béthermin, M., et al. 2012, ApJ, 761, 139
Casey, C. M., Cooray, A., Capak, P., et al. 2015, ApJL, 808, L33
Casey, C. M., Narayanan, D., & Cooray, A. 2014, PhR, 541, 45
Chapman, S. C., Blain, A. W., Ivison, R. J., & Smail, I. R. 2003, Natur, 422, 695
Chapman, S. C., Blain, A. W., Smail, I., & Ivison, R. J. 2005, ApJ, 622, 772
Chapman, S. C., Lewis, G. F., Scott, D., et al. 2001, ApJL, 548, L17
Chiang, Y.-K., Overzier, R. A., Gebhardt, K., et al. 2015, ApJ, 808, 37
Chiang, Y.-K., Overzier, R., & Gebhardt, K. 2013, ApJ, 779, 127
Chiang, Y.-K., Overzier, R. A., Gebhardt, K., & Henriques, B. 2017, ApJL, 844, L23
Clements, D. L., Braglia, F., Petitpas, G., et al. 2016, MNRAS, 461, 1719
Collins, C. A., Stott, J. P., Hilton, M., et al. 2009, Natur, 458, 603
Cox, P., Krips, M., Neri, R., et al. 2011, ApJ, 740, 63
da Cunha, E., Groves, B., Walter, F., et al. 2013, ApJ, 766, 13
Daddi, E., Dannerbauer, H., Stern, D., et al. 2009, ApJ, 694, 1517
Dannerbauer, H., Kurk, J. D., De Breuck, C., et al. 2014, A&A, 570, A55
Downes, D., & Solomon, P. M. 1998, ApJ, 507, 615
Dunlop, J. S., McLure, R. J., Biggs, A. D., et al. 2017, MNRAS, 466, 861
Eales, S., Dunne, L., Clements, D., et al. 2010, PASP, 122, 499
Erb, D. K., Bogosavljević, M., & Steidel, C. C. 2011, ApJL, 740, L31
Evrard, A. E., Bialek, J., Busha, M., et al. 2008, ApJ, 672, 122
Flores-Cacho, I., Pierini, D., Soucail, G., et al. 2016, A&A, 585, A54
Fudamoto, Y., Ivison, R. J., Oteo, I., et al. 2017, MNRAS, 472, 2028
Geach, J. E., Dunlop, J. S., Halpern, M., et al. 2017, MNRAS, 465, 1789
Geach, J. E., Narayanan, D., Matsuda, Y., et al. 2016, ApJ, 832, 37

Gobat, R., Daddi, E., Onodera, M., et al. 2011, A&A, 526, A133
Granato, G. L., De Zotti, G., Silva, L., Bressan, A., & Danese, L. 2004, ApJ, 600, 580
Guidetti, D., Bondi, M., Prandoni, I., et al. 2017, MNRAS, 471, 210
Harrison, I., & Coles, P. 2012, MNRAS, 421, L19
Hilton, M., Stanford, S. A., Stott, J. P., et al. 2009, ApJ, 697, 436
Hodge, J. A., Riechers, D., Decarli, R., et al. 2015, ApJL, 798, L18
Hughes, T. M., Ibar, E., Villanueva, V., et al. 2017, MNRAS, 468, L103
Hung, C.-L., Casey, C. M., Chiang, Y.-K., et al. 2016, ApJ, 826, 130
Ibar, E., Ivison, R. J., Best, P. N., et al. 2010, MNRAS, 401, L53
Iono, D., Yun, M. S., Aretxaga, I., et al. 2016, ApJL, 829, L10
Ivison, R. J., Lewis, A. J. R., Weiss, A., et al. 2016, ApJ, 832, 78
Ivison, R. J., Papadopoulos, P. P., Smail, I., et al. 2011, MNRAS, 412, 1913
Ivison, R. J., Smail, I., Le Borgne, J.-F., et al. 1998, MNRAS, 298, 583
Ivison, R. J., Swinbank, A. M., Smail, I., et al. 2013, ApJ, 772, 137
Ivison, R. J., Swinbank, A. M., Swinyard, B., et al. 2010, A&A, 518, L35
Kennicutt, R. C., Jr. 1998, ARA&A, 36, 189
Kreysa, E., Bertoldi, F., Gemuend, H-P., et al. 2003, Proc. SPIE, 4855, 41
Kubo, J. M., Stebbins, A., Annis, J., et al. 2007, ApJ, 671, 1466
Lapi, A., González-Nuevo, J., Fan, L., et al. 2011, ApJ, 742, 24
Lewis, A. J. R., et al. 2017, arXiv:171108803L
Madau, P., & Dickinson, M. 2014, ARA&A, 52, 415
Matsuda, Y., Nakamura, Y., Morimoto, N., et al. 2009, MNRAS, 400, L66
Matsuda, Y., Yamada, T., Hayashino, T., et al. 2012, MNRAS, 425, 878
Muldrew, S. I., Hatch, N. A., & Cooke, E. A. 2015, MNRAS, 452, 2528
Murphy, E. J., Momjian, E., Condon, J. J., et al. 2017, ApJ, 839, 35
Negrello, M., Gonzalez-Nuevo, J., De Zotti, G., et al. 2017, MNRAS, 470, 2253
Oliver, S. J., Bock, J., Altieri, B., et al. 2012, MNRAS, 424, 1614
Oteo, I., Bongiovanni, A., Pérez García, A. M., et al. 2012a, A&A, 541, A65
Oteo, I., Bongiovanni, A., Pérez García, A. M., et al. 2012b, ApJ, 751, 139
Oteo, I., Ivison, R. J., Dunne, L., et al. 2016b, ApJ, 827, 34
Oteo, I., et al. 2017b, arXiv:170904191O
Oteo, I., et al. 2017c, arXiv:170705329O
Oteo, I., Zwaan, M. A., Ivison, R. J., Smail, I., & Biggs, A. D. 2016a, ApJ, 822, 36
Oteo, I., Zwaan, M. A., Ivison, R. J., Smail, I., & Biggs, A. D. 2017a, ApJ, 837, 182
Overzier, R. A. 2016, A&ARv, 24, 14
Papadopoulos, P. P., & Greve, T. R. 2004, ApJL, 615, L29
Papadopoulos, P. P., Thi, W.-F., & Viti, S. 2004, MNRAS, 351, 147
Pearson, E. A., Eales, S., Dunne, L., et al. 2013, MNRAS, 435, 2753
Planck Collaboration, Ade, P. A. R., Aghanim, N., et al. 2016, A&A, 596, A100
Pope, A., Chary, R-R., Alexander, D. M., et al. 2008, ApJ, 675, 1171
Riechers, D. A., Bradford, C. M., Clements, D. L., et al. 2013, Natur, 496, 329
Riechers, D. A., Carilli, C. L., Capak, P. L., et al. 2014, ApJ, 796, 84
Riechers, D. A., Leung, T. K., Daisy, Ivison, R. J., et al. 2017, ApJ, 858, 1
Romano, D., Matteucci, F., Zhang, Z.-Y., Papadopoulos, P. P., & Ivison, R. J. 2017, MNRAS, 470, 401
Rosati, P., Tozzi, P., Gobat, R., et al. 2009, A&A, 508, 583
Sandberg, A., Guaita, L., Östlin, G., Hayes, M., & Kiaeerad, F. 2015, A&A, 580, A91
Schirmer, M. 2013, ApJS, 209, 21
Schuller, F. 2012, Proc. SPIE, 8452, 84521T
Schuller, F., Menten, K. M., Contreras, Y., et al. 2009, A&A, 504, 415
Scoville, N., Sheth, K., Aussel, H., et al. 2016, ApJ, 820, 83
Shimakawa, R., Kodama, T., Hayashi, M., et al. 2017a, MNRAS, 486, L21
Shimakawa, R., Kodama, T., Hayashi, M., et al. 2017b, MNRAS, 468, L21
Siringo, G., Kreysa, E., Kovács, A., et al. 2009, A&A, 497, 945
Skrutskie, M. F., Cutri, R. M., Stiening, R., et al. 2006, AJ, 131, 1163
Stanford, S. A., Romer, A. K., Sabirli, K., et al. 2006, ApJL, 646, L13
Steidel, C. C., Adelberger, K. L., Dickinson, M., et al. 1998, ApJ, 492, 428
Stevens, J. A., Ivison, R. J., Dunlop, J. S., et al. 2003, Natur, 425, 264
Strandet, M. L., Weiss, A., Vieira, J. D., et al. 2016, ApJ, 822, 80
Swinbank, A. M., Simpson, J. M., Smail, I., et al. 2014, MNRAS, 438, 1267
Swinbank, A. M., Smail, I., Longmore, S., et al. 2010, Natur, 464, 733
Swinbank, A. M., Vernet, J. D. R., Smail, I., et al. 2015, MNRAS, 449, 1298
Tamura, Y., Kohno, K., Nakanishi, K., et al. 2009, Natur, 459, 61
The, L. S., & White, S. D. M. 1986, AJ, 92, 1248
Thomas, D., Maraston, C., Schawinski, K., Sarzi, M., & Silk, J. 2010, MNRAS, 404, 1775
Umehata, H., Tamura, Y., Kohno, K., et al. 2014, MNRAS, 440, 3462
Umehata, H., Tamura, Y., Kohno, K., et al. 2015, ApJL, 815, L8
Venemans, B. P., Röttgering, H. J. A., Miley, G. K., et al. 2007, A&A, 461, 823
Walter, F., Weiß, A., Downes, D., Decarli, R., & Henkel, C. 2011, ApJ, 730, 18
Walter, F., Decarli, R., Carilli, C., et al. 2012, Natur, 486, 233
Wang, T., Elbaz, D., Daddi, E., et al. 2016, ApJ, 828, 56
Weiß, A., De Breuck, C., Marrone, D. P., et al. 2013, ApJ, 767, 88
Weiß, A., Downes, D., Henkel, C., & Walter, F. 2005, A&A, 429, L25
Weiß, A., Henkel, C., Downes, D., & Walter, F. 2003, A&A, 409, L41
Weiß, A., Ivison, R. J., Downes, D., et al. 2009, ApJL, 705, L45
Yamada, T., Nakamura, Y., Matsuda, Y., et al. 2012, AJ, 143, 79
Yang, Y., Zabludoff, A., Tremonti, C., Eisenstein, D., & Davé, R. 2009, ApJ, 693, 1579
Yuan, T., Nanayakkara, T., Kacprzak, G. G., et al. 2014, ApJL, 795, L20
Zeimann, G. R., Stanford, S. A., Brodwin, M., et al. 2012, ApJ, 756, 115
Zhang, Z.-Y., Papadopoulos, P. P., Ivison, R. J., et al. 2016, RSOS, 3, 160025